

# Near-field imaging of Bloch surface waves on silicon nitride one-dimensional photonic crystals

Emiliano Descrovi<sup>1</sup>, Tristan Sfez<sup>2</sup>, Lorenzo Dominici<sup>3</sup>, Wataru Nakagawa<sup>2</sup>, Francesco Michelotti<sup>3</sup>, Fabrizio Giorgis<sup>1</sup> and Hans-Peter Herzig<sup>2</sup>

<sup>1</sup> Dipartimento di Fisica, Politecnico di Torino, corso Duca degli Abruzzi 24, 10129 Torino, Italy

<sup>2</sup> Institut de Microtechnique, Université de Neuchâtel, rue A.-L. Breguet 2, Neuchâtel 2000, Switzerland

<sup>3</sup> Dipartimento di Energetica, SAPIENZA Università di Roma, via A. Scarpa 16, 00161 Roma, Italy

[emiliano.descrovi@polito.it](mailto:emiliano.descrovi@polito.it)

**Abstract:** We perform a near-field mapping of Bloch Surface Waves excited at the truncation interface of a planar silicon nitride multilayer. We directly determine the field distribution of Bloch Surface Waves along the propagation direction and normally to the surface. Furthermore, we present a direct measurement of a near-field enhancement effect under particular coupling conditions. Experimental evidence demonstrates that a  $\sim 10^2$  near-field intensity enhancement can be realistically attained, thus confirming predictions from rigorous calculations.

© 2008 Optical Society of America

**OCIS codes:** (240.6690) Surface waves; (180.5810) Scanning microscopy; (350.4238) Nanophotonics and photonic crystals.

---

## References and links

1. H. Raether, *Surface Plasmons on Smooth and Rough Surfaces and on Gratings*, Tracts in Modern Physics Vol. 111 (Springer, Berlin, Heidelberg, 1988).
2. G. Borstel and H. J. Falge, *Electromagnetic Surface Modes*, edited by A. D. Boardman (Wiley, Chichester, 1982).
3. J. M. Simon, L. I. Perez, and V. A. Presa, "Surface Electromagnetic waves in the interface of an absorbing medium with a uniaxial crystal: comparison between closed solutions and attenuated total reflection," *J. Opt. Soc. Am. A* **13**, 1249-1257 (1996).
4. R. D. Meade, K. D. Brommer, A. M. Rappe, and J. D. Joannopoulos, "Electromagnetic Bloch waves at the surface of a photonic crystal," *Phys. Rev. B* **44**, 10961-10964 (1991).
5. W. M. Robertson, G. Arjavalingam, R. D. Meade, K. D. Brommer, A. M. Rappe, and J. D. Joannopoulos, "Observation of surface photons on periodic dielectric arrays," *Opt. Lett.* **18**, 528-530 (1993).
6. M. Sarrazin and J.-P. Vigneron, "Bounded modes to the rescue of optical transmission," *Europhys. News* **3**, 27-31 (2007).
7. A. V. Kavokin, I. A. Shelykh, and G. Malpuech, "Lossless interface modes at the boundary between two periodic dielectric structures," *Phys. Rev. B* **72**, 233102 (2005).
8. D. Artigas and L. Torner, "Dyakov Surface Waves in Photonic Metamaterials," *Phys. Rev. Lett.* **94**, 013901 (2005).
9. M. Laroche, R. Carminati, and J.-J. Greffet, "Resonant optical transmission through a photonic crystal in the forbidden gap," *Phys. Rev. B* **71**, 155113 (2005).
10. M. Shinn and W. M. Robertson, "Surface plasmon-like sensor based on surface electromagnetic waves in a photonic band-gap material," *Sens. Actuators B* **105**, 360-364 (2005).
11. J. Martorell, D. W. L. Sprung, and G. V. Morozov, "Surface TE waves on 1D photonic crystals," *J. Opt. A: Pure Appl. Opt.* **8**, 630-638 (2006).

12. X. I. Saldana and G. Gonzales de la Cruz, "Electromagnetic surface waves in semi-infinite superlattices," *J. Opt. Soc. Am. A* **8**, 36-40 (1991).
13. A. Y. Cho, A. Yariv, and P. Yeh, "Observation of confined propagation in Bragg waveguides," *Appl. Phys. Lett.* **30**, 471-472 (1977).
14. P. Yeh, A. Yariv, and A. Y. Cho, "Optical surface waves in periodic layered media," *Appl. Phys. Lett.* **32**, 104-105 (1978).
15. P. Yeh, A. Yariv, and C.-S. Hong, "Electromagnetic propagation in periodic stratified media. I. General theory," *J. Opt. Soc. Am.* **67**, 423-438 (1977).
16. F. Ramos-Mendieta and P. Halevi, "Propagation constant-limited surface modes in dielectric superlattices," *Opt. Commun.* **129**, 1-5 (1996).
17. E. Descrovi, F. Frascella, B. Sciacca, F. Geobaldo, L. Dominici, and F. Michelotti, "Coupling of surface waves in highly defined 1D porous silicon photonic crystals for gas sensing applications," *Appl. Phys. Lett.* **91**, 241109 (2007).
18. E. Guillemin, V. Lysenko, R. Orobtcouk, T. Benyattou, S. Roux, A. Pillonnet, and P. Perriat, "Bragg surface wave device based on porous silicon and its application for sensing," *Appl. Phys. Lett.* **90**, 241116 (2007).
19. F. Villa, L. E. Regalado, F. Ramos-Mendieta, J. Gaspar-Armenta, and T. Lopez-Ríos, "Photonic crystal sensor based on surface waves for thin-film characterization," *Opt. Lett.* **27**, 646-648 (2002).
20. R. C. Nesnidal and T. G. Walker, "Multilayer dielectric structure for enhancement of evanescent waves," *Appl. Opt.* **35**, 2226-2229 (1996).
21. G. Tourrel, J. Corset, *Raman Microscopy: Developments and Applications*, (Elsevier Academic Press, 1996).
22. C. Ricciardi, V. Ballarini, M. Galli, M. Liscidini, L. C. Andreani, M. Losurdo, G. Brano, S. Lettieri, F. Gesuele, P. Maddalena, and F. Giorgis, "Amorphous Silicon Nitride: a suitable alloy for optical multilayered structures," *J. Non Cryst. Solid* **352**, 1294-1297 (2006).
23. J. A. Gaspar-Armenta and F. Villa, "Band-structure properties of one-dimensional photonic crystals under the formalism of equivalent systems," *J. Opt. Soc. Am. B* **21**, 405-412 (2004).
24. E. Descrovi, F. Giorgis, L. Dominici, and F. Michelotti, "Experimental observation of optical band-gaps for surface electromagnetic waves in a 1D silicon nitride photonic crystal," *Opt. Lett.* **33**, 243-245 (2008).
25. R. Ulrich, "Theory of the prism-film coupler by plane wave analysis," *J. Opt. Soc. Am.* **60**, 1337-1350 (1970).
26. Our experimental conditions allowed us to factorize the two-dimensional gaussian beam used for sample illumination as indicated by Ulrich [25].
27. E. Bontempi, L. E. Depero, L. Sangaletti, F. Giorgis, and C. F. Pirri, "Growth process analysis of a-Si<sub>1-x</sub>N<sub>x</sub>:H films probed by X-ray reflectivity," *Mat. Chem. and Phys.* **66**, 172-176 (2000).
28. R. Dändliker, P. Tortora, L. Vaccaro, and A. Nesci, "Measuring three-dimensional polarization with scanning optical probes," *J. Opt. A: Pure Appl. Opt.* **6**, S189-S196 (2004).
29. A. Nesci, R. Dändliker, and H.-P. Herzig, "Quantitative amplitude and phase measurement by use of a heterodyne scanning near-field optical microscope," *Opt. Lett.* **26**, 208-210 (2001).
30. P. Tortora, R. Dändliker, W. Nakagawa, and L. Vaccaro, "Detection of non-paraxial optical fields by optical fiber tip probes," *Opt. Commun.* **259**, 876-882 (2006).
31. Y. Wu, M. Villanueva-Ibanez, C. L. Luyer, J. Shen, and J. Mugnier, "Application of multi-wavelength m-lines spectroscopy for optical analysis of sol-gel prepared waveguide thin films," *Proc. SPIE* **5946**, 396-407 (2005).
32. E. F. Y. Kou and T. Tamir, "Excitation of surface plasmons by finite width beams," *Appl. Opt.* **28**, 1169-1177 (1989).
33. A. Huber, N. Ocelic, D. Kazantsev, and R. Hillenbrand, "Near-field imaging of mid-infrared surface phonon polariton propagation," *Appl. Phys. Lett.* **87**, 081103 (2005).
34. W. M. Robertson, "Experimental measurement of the effect of termination on Surface Electromagnetic Waves in one-dimensional photonic bandgap arrays," *J. Lightwave Technol.* **17**, 2013-2017 (1999).
35. A. S. Ramirez-Duverger, J. Gaspar-Armenta, and R. Garcia-Lamas "Surface wave effect on light scattering from one-dimensional photonic crystals," *Opt. Commun.* **277**, 302-309 (2007).
36. L. Li, J. Chandezon, G. Granet, and J. P. Plumey, "Rigorous and efficient grating analysis method made easy for optical engineers," *App. Opt.* **38**, 304-313 (1999).
37. A. Bouhelier and G. P. Wiederrecht, "Surface plasmon rainbow jets," *Opt. Lett.* **30**, 884-886 (2005).
38. F. Kalkum, G. Gay, O. Alloschery, J. Weiner, H. J. Lezec, Y. Xie, and M. Mansuripur, "Surface-wave interferometry on single subwavelength slit-groove structures fabricated on gold films," *Opt. Express* **15**, 2613-2621 (2007).

---

## 1. Introduction

Surface Electromagnetic Waves (SEW) are traveling or stationary waves localized at the interface of two different media. The optical characteristics of the two media determine the kind of SEW that can be sustained. For example, Surface Plasmon Polaritons (SPP) can be coupled at metal/dielectric interfaces (e.g. silver/air and gold/air) in the visible range [1], while Surface

Phonon polaritons can propagate on polar crystals such as SiC at mid-infrared wavelengths [2]. Beside homogeneous, yet anisotropic materials [3], artificial media such as photonic crystals (PC) can sustain SEW [4, 5, 6] at PC-PC [7] or PC-air interfaces [8]. The coupling of surface modes on two-dimensional dielectric PC slabs is also responsible for particular resonant transmission effects [9].

One of the simplest structure allowing coupling and propagation of SEW is constituted by a planar dielectric multilayer or one-dimensional photonic crystal (1DPC) [10, 11]. In general, the ability of PC to sustain surface modes is related to their photonic band structure. For this reason, SEW in truncated periodic photonic crystals are also named Bloch Surface Waves (BSW) and their dispersion curves lay at the edges of or within the forbidden bands [12]. In literature, BSW are also called Tamm states (from solid state physics), surface optical waves and surface photons. The first observations of confined Bloch waves close to the surface of dielectric multilayers are reported in refs. [13, 14]. Contrary to metals, the (generally) low dispersion of the refractive index in dielectric materials allows a larger spectral tunability of BSW as compared to SPP. The layout of the multilayer and the coupling conditions can be optimized in such a way that very narrow reflectance anomalies associated with long-range BSW can be obtained over a wide wavelength range. Furthermore, when BSW are coupled, very intense electromagnetic fields localized at the PC surface can be produced [15, 16]. These particular features make BSW a promising alternative to SPP-based sensing schemes, as demonstrated in some recent work [17, 18, 19].

In this paper, we perform a detailed near-field analysis of a TE-polarized BSW mode coupled to a silicon nitride 1DPC in the Kretschmann configuration. With the help of a multi-heterodyne Scanning Near-field Optical Microscope (SNOM), we estimate the vertical confinement and decay length of a particular BSW mode on the structure surface. Results agree with estimations from far field observations.

An unprecedented direct quantification of the field enhancement associated with BSW is also provided. This near-field analysis allows a direct estimation of the field enhancement without using any supplemental model based on far-field observations [20]. Field enhancement associated with BSW may open opportunities for new applications in domains such as Surface Enhanced Raman Scattering Spectroscopy (SERSS) [21].

## 2. Planar a-Si<sub>1-x</sub>N<sub>x</sub>:H multilayer

A BSW can be coupled to a properly designed 1DPC. The multilayered planar structures are fabricated by Plasma Enhanced Chemical Vapor Deposition (PECVD) on a 500  $\mu\text{m}$  thick Corning glass substrate. The composition of the a-Si<sub>1-x</sub>N<sub>x</sub>:H layers is controlled by varying the ammonia fraction in a SiH<sub>4</sub>+NH<sub>3</sub> plasma. The refractive index is estimated by means of standard optical measurements [22], while their thickness is estimated by calibrating the deposition rate on homogeneous films. The total gas flux and pressure, substrate temperature and electrode distance are set at 75 sccm, 0.35 Torr, 200°C and 20 mm, respectively.

The multilayer is composed of a 10-period stack of high ( $n_H = 2.23$ , at  $\lambda = 1530$  nm) and low ( $n_L = 1.75$ , at  $\lambda = 1530$  nm) refractive index layers having thicknesses  $d_H = 240$  nm and  $d_L = 294$  nm, respectively (see Fig. 1(a)). A low-index layer constitutes the top layer of the truncated 1DPC. The band diagram associated to an infinite stack of layers is presented in Fig. 1(b). The abscissa axis is referred to the propagation constant  $\beta$  of light guided within the structure. The white regions indicate forbidden bands, while the dashed lines represent the dispersion relations  $\omega = \beta c$ ,  $\omega = \beta/n_H c$ ,  $\omega = \beta/n_L c$  of free photons propagating in vacuum, in the high and low refractive index layers respectively. If we consider a truncated, semi-infinite 1DPC, the dispersion curve of BSW can be directly calculated. In the past, several computational methods have been proposed to this aim (see e.g. [23] and references therein). With the help of a well-

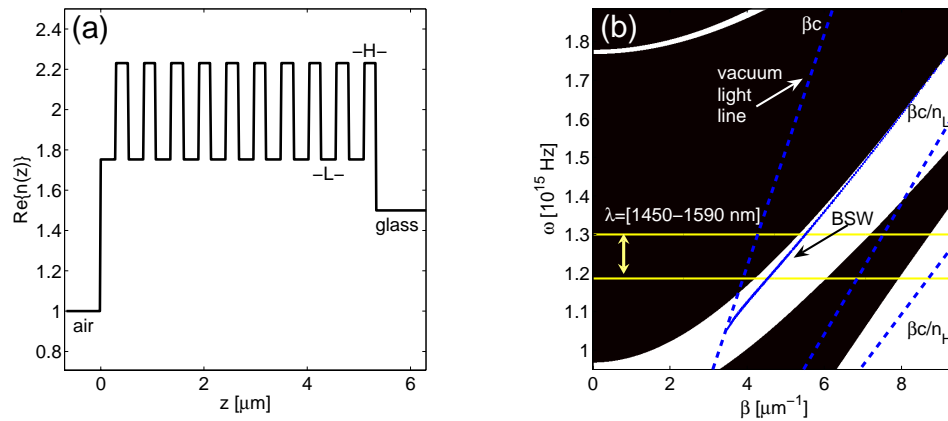


Fig. 1. (a) Refractive index profile of the multilayer deposited on a glass substrate; (b) Calculated band diagram (TE polarization) of a 1DPC consisting of an infinite sequence of high ( $n_H = 2.23$ ) and low ( $n_L = 1.75$ ) refractive index layers  $d_H = 240$  nm and  $d_L = 294$  nm respectively. The white regions indicate the forbidden bands. BSW dispersion curve associated to a semi-infinite 1DPC is explicitly indicated.

known matrix method [15], we found that a BSW laying in the first forbidden band, slightly beyond the vacuum light line, can be coupled at the 1DPC-air interface.

### 3. Far-field characterization

#### 3.1. Ellipsometric setup

Coupling conditions for BSW can be determined on the basis of a far-field characterization. For this purpose, we employ an ellipsometric setup implementing a Kretschmann-Raether spectroscopic configuration as shown in Fig. 2.

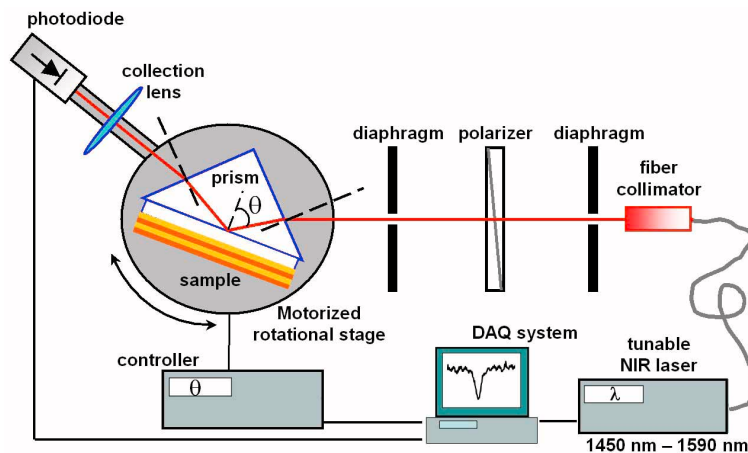


Fig. 2. Sketch of the ellipsometric setup in the Kretschmann-Raether configuration used for the far-field characterization of BSW coupled to the silicon nitride 1DPC.

A collimated and TE-polarized beam is expanded from a fibered, tunable diode laser source

(Nettest, Tunic-Plus) and used to illuminate the sample through the input facet of a 45 degree BK7 glass coupling prism ( $n_p = 1.501$ ). The angular divergence of the illuminating beam is estimated to be  $\delta = 0.038$  deg. The sample is contacted to the prism facet by means of a proper index matching oil. Reflectance profiles at fixed wavelengths are obtained by means of a single channel detection scheme, in which the sample is rotated with respect to the incident beam. The parameter  $\theta$  is the angle between the normal to the 1DPC planar interfaces and the direction of the incident beam at the prism/multilayer interface. A low numerical aperture lens collects and focuses the reflected light onto the photodiode. The collection lens and photodiode are rotated accordingly as the angular orientation of the sample is varied.

### 3.2. Determination of BSW propagation constant and attenuation length

In the Kretschmann configuration, the propagation constant  $\beta$  of guided modes propagating in the structure can be calculated by using the following formula:  $\beta = 2\pi n_p \sin\theta / \lambda$ , where the incidence angle  $\theta$  of the incoming light is considered at the multilayer/glass interface. After considering the band diagram shown in Fig.1(b), we expect to couple BSW in the first forbidden band at incidence angles slightly larger than the critical angle.

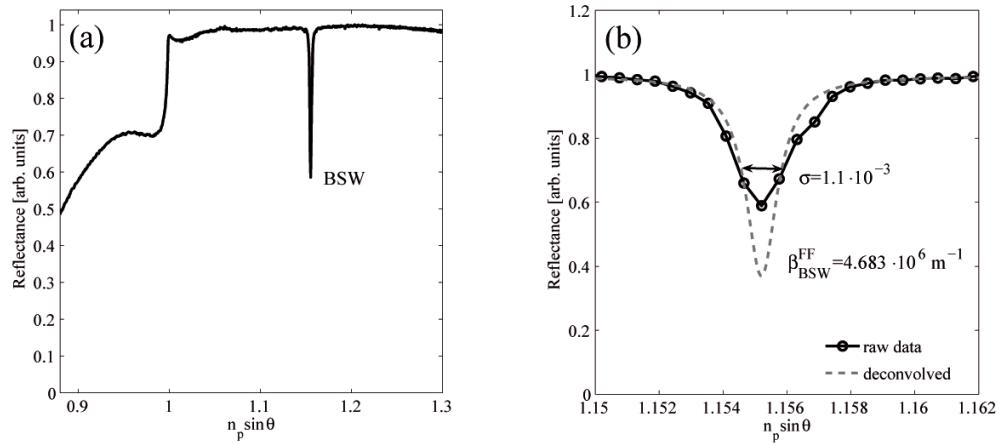


Fig. 3. (a) Experimental far-field angular reflectance in the Kretschmann configuration; (b) Reflectance anomaly associated with BSW coupling (raw and deconvolved data).

The full BSW dispersion curve in the wavelength range 1450-1590 nm has been published previously [24]. In Fig. 3 we present the angular reflectance profile measured at a fixed wavelength  $\lambda_{BSW} = 1550$  nm. The angular position of the cusp in Fig. 3(a) lies on the light line in vacuum  $\omega = \beta c$  shown in Fig.1(b), while the sharp dip represents a reflectance anomaly indicating coupling to BSW. The dip is centered at an angle  $\theta_{BSW}$  such that  $n_p \sin\theta_{BSW} = 1.1553$ , therefore the propagation constant estimated by means of far-field measurements is  $\beta_{BSW}^{FF} = n_p \sin\theta_{BSW} \cdot 2\pi / \lambda_{BSW} = 4.683 \mu\text{m}^{-1}$ . No reflectance dip is observed if the illuminating beam is TM-polarized.

As described by Ulrich in Ref. [25], the bandwidth of reflectance anomalies can be used to calculate the decay length of prism-coupled waveguide modes. Nevertheless, a significant broadening of the measured reflectance dips may occur due to the angular divergence of the illuminating beam. In fact, for given coupling strength conditions, the measured reflectance anomalies result from a convolution of the waveguide transfer function with the angular spectrum of the incident beam. In our setup, we use a gaussian beam estimated to have an angular di-

vergence of  $\delta \simeq 0.038$  deg. and a waist  $w_0 = \lambda/\pi\delta \simeq 744 \mu\text{m}$ . In order to remove the influence of the finite size of the illuminating beam, we perform a one-dimensional deconvolution of the measured reflectance anomaly by the beam angular spectrum [26] and find out the Lorentzian profile shown in the dashed curve of Fig. 3(b). The full bandwidth of the deconvolved profile is  $\sigma = 1.1 \cdot 10^{-3}$  and approximates the BSW losses with a plane-wave excitation. The far-field estimation of the BSW decay length is  $L_{BSW}^{FF} = (\pi\sigma/\lambda_{BSW})^{-1} = 448.5 \mu\text{m}$ . The decay of the mode along the propagation direction is caused by absorption by the material, surface scattering and leakage into the prism. Nevertheless, due to the low absorption of silicon nitride in the Near-InfraRed (NIR) range and the low roughness of the multilayer surface [27], the BSW is mainly attenuated by light leakage into the prism.

Once the BSW decay length is known, an estimation of the coupling strength can be performed. We consider the ratio  $L_{BSW}^{FF}/w_0 = 0.634$  as a coupling parameter, demonstrating that the far-field measurements are conducted under coupling conditions close to the optimum [25]. This allows a rather large fraction of the incident power to be transferred to the BSW and be guided with low losses.

## 4. Near-field mapping of BSW

### 4.1. Multi-heterodyne Scanning Near-field Optical Microscope

A heterodyne SNOM [28] is a modified SNOM where the detection is based on an interferometric technique. The signal and reference channels are both frequency shifted. By demodulating the resulting beat signal, we can retrieve the amplitude and the phase of the optical field captured by the probe. Multi-heterodyne SNOM is an extension of this principle. Two orthogonally polarized references as well as two orthogonal signals are generated at different frequencies [29]. In this way, it is possible to obtain the amplitudes and phases related to both polarizations during a single scan. A similar setup has been successfully employed to investigate the coupling mechanism of non-paraxial optical fields (visible range) into transparent SNOM tips [30]. In this work, a multi-heterodyne interferometer coupled to a fibered collection-mode SNOM is used.

In Fig. 4, a schematic drawing of the setup is presented. Blue paths correspond to Polarization-Maintaining Fibers (PMF) and yellow paths to Single Mode Fibers (SMF). The fibered output of a tunable laser source (Agilent 81682A, spectral range 1460-1580 nm) is sent through a polarization controller, and then onto a Polarizing Beam Splitter (PBS). The power ratio between the two linearly polarized outputs of the PBS is tuned by adjusting the polarization controller. The first output constitutes the signal channel and is used for sample illumination. The second output is the reference channel. Each channel is split by a 50/50 splitter and each of the 4 resulting beams are labeled by means of an Acousto-Optic Modulator (AOM) used as a frequency shifter. Both signal beams are then recombined in a PMF by means of a PBS in such a way that they are aligned along the slow and fast axes of the fiber. The slow and fast fiber axes are oriented perpendicularly and parallel to the multilayer surface respectively. In this configuration, the 1DPC is simultaneously illuminated by both TE and TM-polarized beams, having an almost equivalent intensity. The fiber output can be either collimated or focused by snap-on lenses. With the help of a PBS, the reference beams are recombined in a SMF. Orthogonality of the reference beam is well preserved up to the detector and of the signal beam up to the sample.

As shown in Fig. 4, illumination is provided by either a FC/APC receptacle-style focuser or a collimator. The focuser focal length and magnification are  $f=20$  mm and  $M=1.7$  respectively, which gives a numerical aperture  $NA \simeq 0.065$ . The focuser and collimator are mounted on a goniometric stage placed on a 3-axis translation stage. A 45 degree BK7 prism holds the sample and appropriate index matching fluid is used. The reflected light is detected by an IR-sensitive CCD camera arranged in a standard single wavelength M-line setup [31].

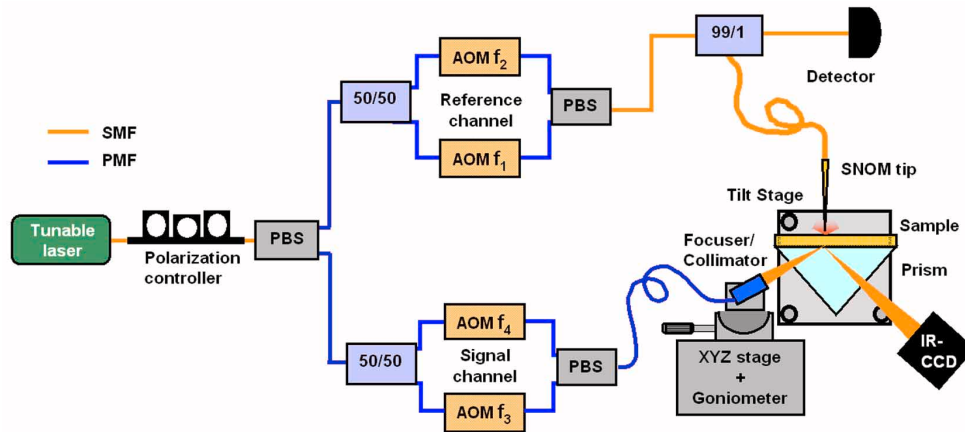


Fig. 4. Schematic diagram of the multi-heterodyne SNOM setup used for the near-field characterization of BSW coupled to silicon nitride 1DPC.

After interacting with the sample, light is collected by the SNOM probe (Lovalite, 70 nm Al coated, aperture 200 nm) and mixed with the reference channel using a 99/1 coupler before being detected by a photodiode. The detected signal is hence a superposition of the four frequency shifted beams, which leads to six beat components. The amplitudes and phases of the optical near-fields are then lock-in detected. Scans are performed by moving the SNOM tip on the sample surface in shear-force configuration (SNOM Control Unit, APE Research).

With this setup it is possible to simultaneously map the TE and TM polarized evanescent fields generated by the two orthogonally polarized illuminating beams at the sample surface.

#### 4.2. BSW near-field distribution and related analysis

We focus the combined TM and TE polarized beam on the multilayer surface through the coupling prism. The beam wavelength and incidence angle were  $\lambda = \lambda_{BSW}$  and  $\theta = \theta_{BSW}$  respectively. The multilayer is designed in such a way to couple only TE-polarized light to BSW in the 1450-1590 nm spectral range. For this reason, the near-field distributions associated with the two orthogonal polarizations are expected to be different at the 1DPC surface, the TM-polarized light being evanescent because of Total Internal Reflection (TIR). The multi-heterodyne detection system allows a simultaneous mapping of both fields in a single scanning process. Near-field intensity maps generated at the 1DPC surface upon incident TM and TE polarized light are presented in Fig. 5(a) and Fig. 5(b), respectively. A normalization is performed with respect to the intensity maximum of the TE-polarized field.

The tip-sample distance is controlled by means of a shear-force-based feedback system working in constant-height mode. The SNOM tip is kept in close proximity to the sample surface during the scanning process. The shear-force error map shown in Fig. 5(c) reveals the presence of topographic defects on the sample surface.

The three-axis piezo-scanner of the microscope allows a maximum lateral scan size of  $100 \times 100 \mu\text{m}$ . Larger scans are performed by coarse adjustment of the sample position with respect to the tip and stitching of the resulting SNOM images.

The near-field maps provide direct evidence of BSW coupling. The TM-polarized field appears as a deformed Airy pattern. In the focal plane of the incident focused beam, the optical field has an Airy-like distribution, because of diffraction at the focuser entrance pupil. The ob-

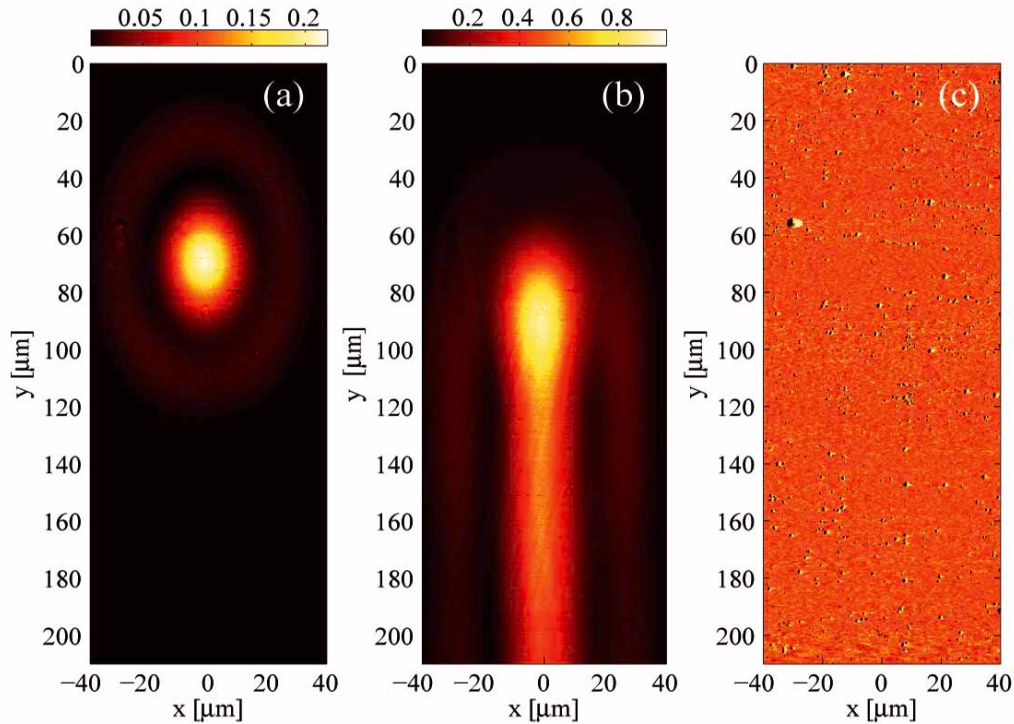


Fig. 5. Two dimensional intensity maps of the optical near-field at the 1DPC surface collected by the multi-heterodyne SNOM: (a) TM-polarization, (b) TE-polarization. Illumination wavelength  $\lambda_{BSW} = 1550$  nm, incidence angle  $\theta = \theta_{BSW}$ . (c) Shear-force error signal map.

served elongation is due to the combined effect of refraction at the prism input facet and the geometrical projection of the focused incident beam onto the 1DPC surface. The horizontal spot size gives an indication of the beam waist within the prism:  $w_0 \simeq 11.4 \mu\text{m}$ . In contrast, the TE-polarized field appears as a comet-like pattern. We identify a radiation coupling region, where an elongated Airy-like distribution showing a strong, asymmetric deformation in the  $y$  direction is observed. Far from the coupling region, a low divergence ‘comet tail’ reveals BSW propagation.

A more detailed analysis of the near-field distribution can be conducted by considering cross-sectional field distributions. In Fig. 6 we show the normalized amplitudes of both the TE and TM fields along the line  $x = 0$  (the propagation axis of the BSW).

The shift of the TE-polarized amplitude maximum in the forward direction with respect to the TM-polarized maximum highlights the resonant coupling of BSW. In the case of a purely gaussian incident beam, such a shift monotonically increases as the coupling strength diminishes. In particular, for a coupling parameter  $L_{BSW}^{FF}/w_0 = 448.5/11.4 \simeq 40$ , Ulrich [25] predicts a positive shift of the intensity maximum  $y_M^{theory} \sim 1.7 \cdot w_0 = 19 \mu\text{m}$  which is rather close to the experimentally observed  $y_M^{exp} \simeq 22 \mu\text{m}$ .

One effect due to weak coupling is the tiny near-field enhancement associated with the prism-coupled surface modes [32]. We observe a BSW amplitude maximum  $\sim 2.5$  times as large as compared to the TM-polarized TIR field. In the next section we will show that the BSW near-field intensity can be greatly enhanced by means of a collimated beam increasing the coupling

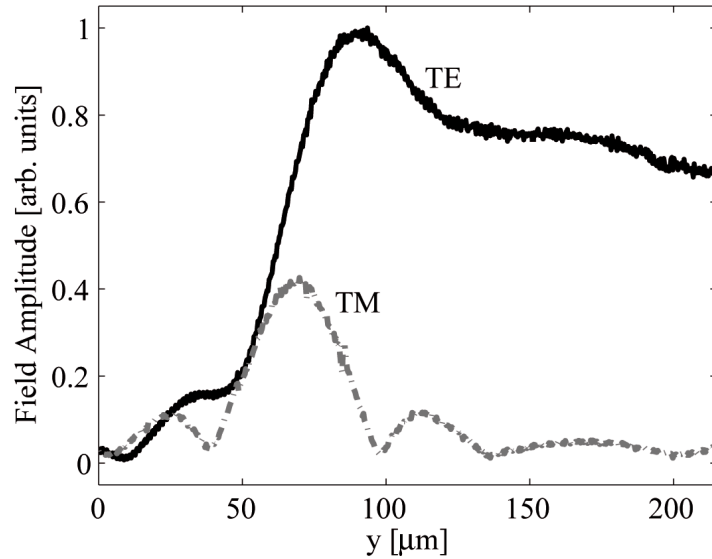


Fig. 6. Cross sectional normalized amplitude distribution of the TE and TM polarized near-fields on the IDPC surface measured along the line  $x = 0$ .

strength.

Far from the coupling region, where no direct illumination is present, the traveling BSW is slowly attenuated because of several loss mechanisms. In this case, the field distribution in the propagation direction can be described by means of decreasing exponential functions.

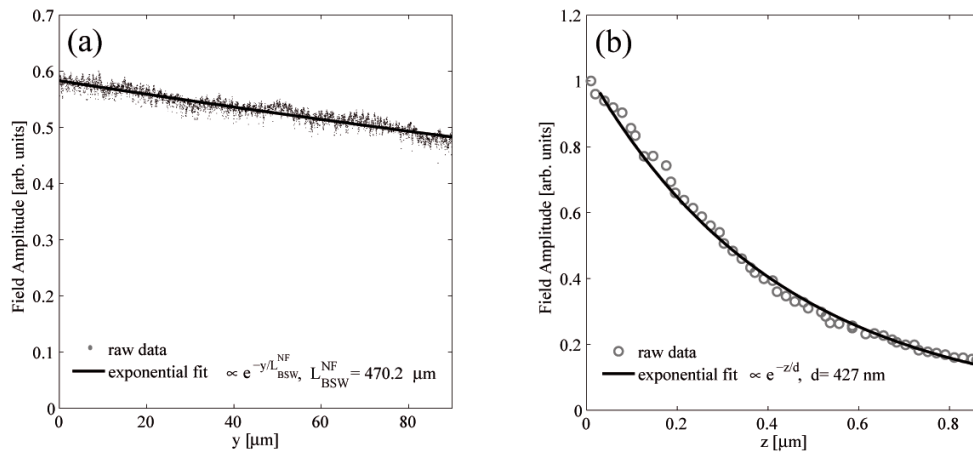


Fig. 7. (a) Amplitude profile of the BSW along the propagation direction. Best exponential fit returns a decay length  $L=470.2 \mu\text{m}$ ; (b) Amplitude profile of BSW as a function of distance from the IDPC surface. Best exponential fit returns a decay distance  $d=427 \text{ nm}$ .

In order to estimate the BSW decay length, we perform a one-dimensional scan, detecting near-field amplitude  $A(y)$  and phase  $\Phi(y)$  along a  $90 \mu\text{m}$  long line at  $x = 0$ , in the comet tail region. As shown in Fig. 7(a), the BSW amplitude is gradually decreasing in the propagation direction. Due to the low absorption of silicon nitride in the NIR region, the losses are essen-

tially due to light coupling into the prism. Moreover, the surface mode is only weakly scattered by the film roughness and remains tightly confined to the sample surface (Fig. 7(b)). Best-fit curves to the measured near-field amplitude profiles shown in Fig. 7 indicate an attenuation length  $L_{BSW}^{NF} = 470.2 \mu\text{m}$  in the propagation direction and a decay distance  $d = 427 \text{ nm}$  normal to the 1DPC surface. The slightly larger value of  $L_{BSW}^{NF}$  with respect to  $L_{BSW}^{FF}$  may be due to the presence of some residual direct illumination in the scanned region.

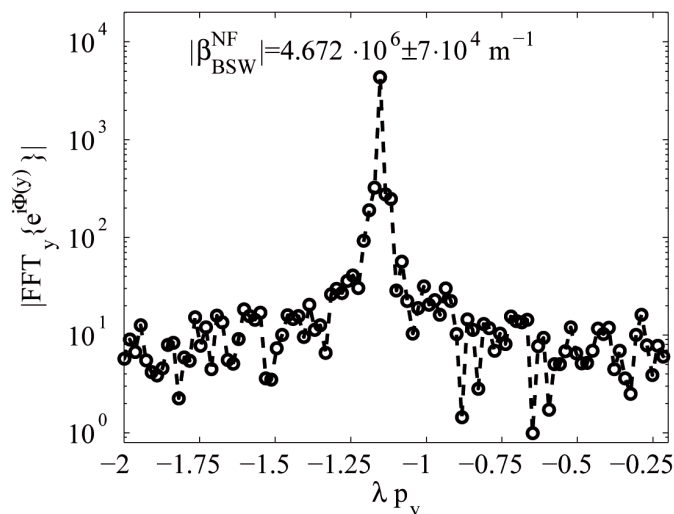


Fig. 8. One dimensional Fourier Transformation (absolute value) of the complex term  $\exp[i\Phi(y)]$  for the TE-polarized field in the comet tail region.

In some recent work, the propagation constants of surface waves have been retrieved from heterodyne near-field measurements (see e.g. Ref. [33]). We perform a one-dimensional Fourier Transform (FT) of the complex term  $\exp[i\Phi(y)]$ , calculated from the phase  $\Phi(y)$  previously measured.

The spatial frequency variable  $p_y$  is derived from the sampling interval  $\Delta y = 177 \text{ nm}$ . The absolute value of the Fourier spectrum as a function of the dimensionless variable  $\lambda p_y = n_p \sin\theta$  is shown in Fig. 8. The large amplitude and the frequency position of the main peak indicate that, far from the coupling region, the TE-polarized near-field is essentially harmonic, with a spatial frequency  $\beta_{BSW}^{NF} = 2\pi p_y = 4.672 \pm 0.07 \mu\text{m}^{-1}$ . The rather large width of the peak is a spurious effect due to improper truncation of the signal in the real space which brings a non-integer number of wave periods into the FT operation. The uncertainty in the determination of  $\beta_{BSW}^{NF}$  is estimated on the basis of the frequency resolution  $2\pi/90 \mu\text{m}^{-1}$ . The difference between  $\beta_{BSW}^{NF}$  and  $\beta_{BSW}^{FF}$  evaluated in the far-field falls within the bands of experimental error.

## 5. Enhanced near-field intensity

It is well known that the amplitude of the electromagnetic field is strongly dependent on the vertical confinement of BSW on the PC surface. It has been shown that an increase of such a confinement can be obtained by a proper tailoring the last PC layer, thus resulting in an electromagnetic field enhancement factor of several orders of magnitude [34, 35].

In a given layered structure, the coupling strength determines the power density distribution of coupled modes as well as the maximum intensity value within the guiding medium or at the structure boundaries. In the previous section we managed to weakly couple BSW by means of

a focused incident beam (waist  $w_0 = 11.4 \mu\text{m}$ ) in such a way that a slowly decaying guided mode was observed far from the directly illuminated coupling region. Nevertheless, the near-field enhancement associated with the BSW was rather small.

To observe more directly this enhancement effect, we prism-coupled a BSW at  $\theta = \theta_{BSW}$  using a collimated beam for illumination (divergence  $\delta = 4 \text{ mrad}$ , waist  $w_0 = \lambda/\pi\delta = 120 \mu\text{m}$  at  $\lambda = 1550 \text{ nm}$ ). In this configuration, the coupling parameter at  $\lambda = 1550 \text{ nm}$  diminishes to  $L_{BSW}^{NF}/w_0 = 470.2/120 \simeq 3.9$  and a strong increase in the near-field intensity is expected. We place the SNOM tip in interaction with the surface and keep it at a fixed position on the sample while the tunable laser wavelength is scanned. During the wavelength sweep, the near-field intensity spectrum as detected by the SNOM tip is measured for both the TE and TM polarizations. The incidence angle is set in such a way that a near-field intensity maximum is obtained at  $\lambda = 1550 \text{ nm}$ . The measurement results are reported in Fig. 9.

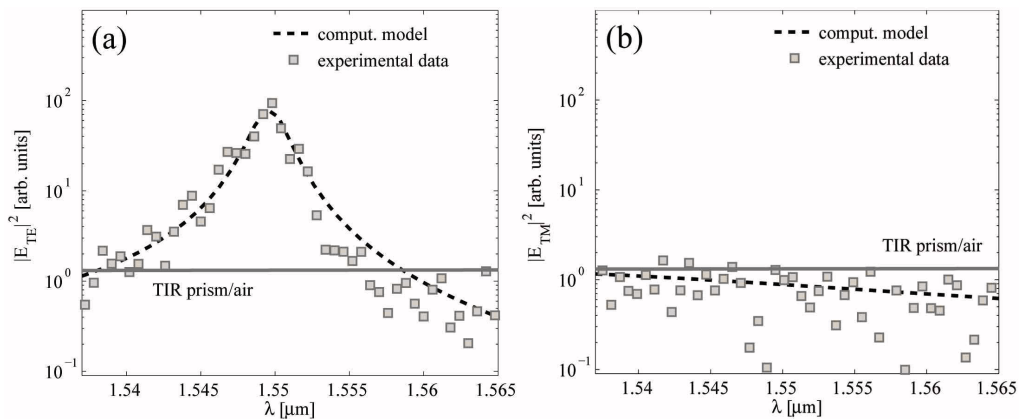


Fig. 9. Near-field intensity spectrum of (a) a TE and (b) a TM-polarized evanescent field on the 1DPC surface. The polarization-dependent field-enhancement effect is associated with the excitation of a TE-polarized BSW. For comparison purposes, the near-field spectrum of a simple glass/air interface illuminated under TIR conditions at a fixed angle is also shown (gray line in both figures).

The absolute TE and TM near-field intensities can be directly compared. We observe that the near-field spectrum for the TE polarization shows a peak at approximately  $\lambda = 1550 \text{ nm}$ , where the detected intensity is almost two orders of magnitude larger than for the corresponding TM case.

In addition to the experimental measurements, we rigorously calculate the near-field intensity spectrum generated by a one-dimensional gaussian beam having waist  $w_0 = \lambda/\pi\delta$  and wavelength  $\lambda \in [1535 - 1565] \text{ nm}$  using the well known C-method [36]. In our computational model, we consider the proper incidence angle for having BSW coupling at  $\lambda = 1550 \text{ nm}$ . In the case of a simple stack of planar layers, modal methods like the C-method can be used to numerically implement a simple transfer matrix algorithm. We consider a Kretschmann geometry in which a set of plane waves belonging to the angular spectrum of the incident gaussian beam illuminates the multilayered structure. Finally, the calculated electric fields for each angular spectrum component are coherently summed. These results are shown with the experimental data in Fig. 9. Note that the calculated spectra are normalized by an arbitrary factor obtained by best fitting to the experimental data. We only consider the TE case in the fit process: the calculated near-field TM-polarized spectrum is normalized by the same factor.

The near-field spectrum for the TE polarization shows a fairly well-defined resonant

Lorentzian shape, whose width and height well matches the measured profile. At the 1DPC surface, the maximum intensity peak at  $\lambda = 1550$  nm is more than  $10^2$  times the intensity predicted for a simple glass/air interface. This measurement directly demonstrates the effect of near-field enhancement on the surface of properly designed photonic structures. It is interesting to remark that, outside the BSW resonance region, the near-field intensity is smaller than in the case of a glass/air interface. This is due to the presence of the photonic structure, which is a dielectric multilayer mirror and more strongly attenuates the (evanescent) light tunneling to the surface of the device. A similar effect also applies to the TM-polarized field.

## 6. Conclusion

In this paper we presented a near-field study of a BSW coupled on one-dimensional silicon nitride photonic crystals. Our work allowed us to gain insight on several interesting aspects of BSW coupling and propagation.

A BSW can be weakly coupled on a 1DPC by means of a moderately focused TE-polarized beam in the Kretschmann configuration. Similarly to surface plasmons on metallic films [37], the near-field spatial distribution of the mode shows an Airy-like coupling region due to the distortion of the direct beam illumination in the BSW forward direction. The Fourier analysis based on the measured mode phase showed that, far from direct illumination, only the k-component matching the  $\beta$  of the BSW mode survives. The BSW decay constant estimated by the near-field measurements is  $L_{BSW}^{NF} \simeq 470$   $\mu$ m. Attenuation is mainly due to radiation leakage through the prism rather than material absorption and can be drastically reduced by propagating the BSW on free guiding structures with no prism. Unfortunately, the spatial frequency resolution of the SNOM did not allow us to separately investigate the transient behavior of those evanescent k-components coupled by the incident beam but not perfectly matching the BSW propagation constant [38].

If BSW are more strongly coupled, an evident field enhancement in the near-field is observed. By using a collimated beam, we managed to generate a near-field over 100 times as intense as the evanescent field at a glass/air interface. These results make surface waves coupled on dielectric multilayers an interesting alternative to surface plasmons in sensing applications based on enhanced Raman or fluorescence spectroscopy. In this latter case, the use of dielectric materials instead of metals may strongly reduce luminescence quenching effects due non-radiative energy transfer to metallic surfaces.

This work is supported by the Centre of Excellence funded by MIUR (Italian Ministry for Education, University and Research) LATEMAR (grants - FIRB 2003-2004) and the Swiss National Science Foundation.